Journal of Alloys and Compounds, Volume 936, March 2023, Article number 168307
DOI:10.1016/j.jallcom.2022.168307

Densification mechanism of Ti-Al-Nb alloys pressurelessly sintered from Al-Nb master alloy powder for cost-effective manufacturing

Xuzhen Liu [a], Jun Wang [b], Yanmo Li [c], Shukui Li [a,d,e], Qi Cai [a,*]

[a] *School of Materials Science and Engineering, Beijing Institute of Technology, Beijing 100081, China*

[b] *Welding Engineering and Laser Processing Centre, Cranfield University, Bedfordshire, MK43 0AL, UK*

[c] *Luoyang Ship Material Research Institute, Luoyang 471023, China*

[d] *China National Key Laboratory of Science and Technology on Materials under Shock and Impact, Beijing Institute of Technology, Beijing 100081, China*

[e] *State Key Laboratory of Explosion Science and Technology, Beijing Institute of Technology, Beijing, 100081, China*

* Corresponding author. Email: caiqi6406608@163.com.

Abstract

Pressureless sintering is a cost-effective method to fabricate shaped Ti-Al-Nb alloy components in the aerospace industry. However, the sintering pores in the Ti-Al-Nb alloys led to inferior mechanical properties when using elemental Al powder as the raw material. By completely replacing the Al powder with the Al-Nb master alloy powder, the pores were substantially reduced in the pressurelessly sintered Ti-22Al-17.5Nb (at.%) alloy, accompanied by the improvement of the tensile strength. We investigated the densification mechanisms by implementing the isothermal quenching experiments at 500-1200 ºC. In the Ti/Al/Nb compact, the pores originated from the melting of Al and the Kirkendall effect at the interfaces of the Ti_3Al and Nb particles. The transitions of $Ti+3Al \rightarrow TiAl_3$ and $\alpha_2 \rightarrow B2$ determined the porosity of the sintered alloy. In the Ti/Al-Nb/Nb compact, the Kirkendall pores at the Ti/Al_3Nb interfaces were reduced since the diffusion of Al in Ti was

retarded. The accelerated diffusion of Nb in Ti_3Al suppressed the Kirkendall effect at the Nb/Ti_3Al interfaces and promoted the formation of the B2 phase. The ripening of the B2 grains further contributed to the densification of the sintered alloy.

Keywords Ti-Al-Nb alloy; pressureless sintering; powder metallurgy; phase transition; densification.

1. Introduction

With the increasing demand for long traveling distances and high carrying capacities in aircraft and spacecraft, lightweight and high-strength alloys are required to improve the thrust-to-weight ratio and the combustion efficiency of aerospace engines. In addition to the nickel-based superalloy, titanium alloys have attracted considerable attention due mainly to their high specific strength, superior high-temperature strength, and excellent corrosion resistance [1, 2]. Among the classic Ti alloys, the intermetallic Ti-Al alloys exhibit high strength at 600-750 ^{o}C, since the internal atoms are in long-range order [3]. However, the intrinsic brittleness [4] of the Ti-Al alloys limited their engineering applications. By incorporating 15-27 at.% Nb, the room-temperature ductility and fracture toughness of the Ti-Al alloys were successfully improved [5, 6]. Ever since Banerjee et al. identified the orthorhombic Ti_2AlNb (O) phase in the Ti-22Al-12.5Nb (at.%, similarly below) alloy [7], various Ti_2AlNb-based alloys were developed as lightweight and high-temperature structural materials [8-11]. Although multiple processing methods were employed, the deformation ability was barely improved for the Ti_2AlNb-based alloys, and the deformation processing condition for the shaped pieces was still harsh. When a large-scale component of the Ti_2AlNb-based alloy was fabricated by smelting, macrosegregation was hardly avoided due to the high alloying degree. Hence, the smelting and deformation processing techniques are not applicable to produce the components of

the Ti_2AlNb-based alloy in irregular shapes, e.g., cartridge receiver, impeller, and blisk in aerospace engines.

Powder metallurgy, a near-net-shaped technique, was used to prepare the Ti_2AlNb-based alloys [12, 13]. The components in irregular shapes were fabricated without severe deformation, and uniform composition and refined grains were obtained [14]. At present, the Ti-Al-Nb alloys are primarily prepared from stoichiometric pre-alloyed powder by pressure-assisted sintering methods [12, 15, 16], among which hot isostatic pressing (HIP) and spark plasma sintering (SPS) are widely used. Zhang et al. demonstrated that the Widmanstätten structure formed in the Ti_2AlNb-based alloys HIPped at 1150 °C and under 120 MPa, and the alloys exhibited the ultimate tensile strength of 910 MPa and an elongation of 4.8% at 650 °C [17]. Wang et al. fabricated Ti_2AlNb sheets via SPS and hot-packed rolling. The ultrafine O phase, uniformly distributed in the B2 matrix, resulted in a tensile strength of 1239 MPa and an elongation of 6.47% [18]. As cartridge receivers and impellers were successfully manufactured from the pre-alloyed powder by HIP [19], cost reduction and mass production became the main concerns in industries. The critical issues lay in the costly Ti_2AlNb pre-alloyed powder and the dependence on the custom sheath.

The cost-effective elemental powders could be pressed into a designed shape at room temperature, and the Ti-Al-Nb alloys were then prepared by sintering the compacts [20-24]. However, high pressure was necessary to guarantee the density of the alloys. To date, pressureless sintering was barely used to fabricate the Ti-Al-Nb alloys from elemental powders. Kayani et al. sintered the Ti-48Al-2Nb alloy from the elemental powder at 1200 ºC and atmospheric pressure. The porosity of the sintered alloy reached 23.9% [25], and the mechanical properties were unreported. The high porosity was the main disadvantage for the pressurelessly sintered Ti-Al-Nb alloys, which might lead to low

mechanical properties [23].

To improve the density of the pressurelessly sintered Ti alloys, TiH_2 was used as one of the raw materials in most studies [24, 26]. In contrast with the alloy prepared from Ti powder, the ones from TiH_2 powder showed higher density and improved mechanical properties. The densification process was strongly associated with the phase transitions upon heating. Zhao et al. attributed the densification mechanism to the diffusion of Ti and Nb in the Ti-Nb alloys, and the sintering temperature and the period determined the degree of densification [27]. Liang et al. elucidated the relationship between the pores and the phase transitions throughout the sintering process of the Ti-48Al-6Nb alloy. The solid-state reactions of $3TiAl_3+2Nb \rightarrow 2NbAl_3+3TiAl$, $TiAl+2Ti \rightarrow Ti_3Al$, and $NbAl_3+5Nb \rightarrow 3Nb_2Al$ contributed to the densification of the alloy [28].

Although TiH_2 was beneficial to the densification of the Ti alloy, cracks would form in the sintered alloys due to the escape of H_2. Therefore, the heating rate must be strictly controlled as slow as 5 $^{o}C \cdot min^{-1}$ at the dehydrogenation stage, and the sintering cost will increase. According to previous studies, decreasing the diffusion rate of Al and increasing that of Nb are critical elements for the densification of Ti-Al-Nb alloys. A possible route was to replace the Al powder with Al-Nb alloy powder as the raw material. Wang et al. fabricated the Ti-23Al-17Nb alloy from the TiH_2, Nb-Al, and Al powders by pre-treatment, cold isostatic compressing (CIP), and pressureless sintering at 1200 ^{o}C for five hours, The density of the alloy reached 98.7%. The strength and elongation of the alloy reached 941 MPa and 11.7%, respectively [29]. Nevertheless, the TiH_2 and Al powders were still used as raw materials, which would lead to cracks in the alloys.

In this study, we used the Al-Nb master alloy powder to replace the Al powder as the raw material, and dense Ti-Al-Nb alloys were prepared from Ti, Al-Nb, and Nb powder by cost-effective

pressureless sintering. The room- and high-temperature mechanical properties were measured to confirm the effectiveness of this fabrication method. The densification mechanism was illustrated by systematically analyzing the phase transitions and microstructure evolution during sintering. This study provides a foundation for the cost-effective fabrication of the Ti-Al-Nb alloys, and the initial experimental results encourage one to apply the pressureless sintering method on other Ti alloys for cost-effective industrial production.

2. Experimental details

The Ti-Al-Nb alloy (AlNb#2) with a nominal composition of Ti-22Al-17.5Nb (at.%) was prepared from Ti (~45 μm, 99.9% in purity), Al-Nb master alloy (20-30 μm, 99.9% in purity), and Nb (5-10 μm, 99.9% in purity) powders. A reference alloy (Al#1) was prepared from Ti (~45 μm μm, 99.9% in purity), Al (5-10 μm, 99.9% in purity), and Nb (5-10 μm, 99.9% in purity) powders. The raw material powders were mixed in a planetary ball mill, and the mixture was filled into reusable cylindrical rubber packages on a vibration device. Fig. 1 shows the SEM images of the ball-milled powders, as well as the corresponding element mappings. By completely replacing the Al powder with the Al-Nb master alloy powder, the homogeneity of Ti (Fig. 1b and f) and Al (Fig.1c and g) in the mixture hardly changed after the planetary ball mill. Since fewer Nb particles were included in the Ti/Al-Nb/Nb mixture, the homogeneity of Nb was improved by using Al-Nb master alloy powder as the raw material. Most areas of Nb overlapped with those of Al in the mixture of Ti, Al-Nb, and Nb powders (Fig. 1d and h). The sealed rubber packages were molded by cold isostatic pressing at 300 MPa, and the shaped compacts were sintered at 1400 ^{o}C for four hours with a heating rate of 10 $^{o}C \cdot min^{-1}$ in a pipe furnace (Tianjin Zhonghuan SK-G10163) under Ar atmosphere. Fig. 2 shows the reproduced Ti-22Al isopleth using the thermodynamic data of Cupid et al. [30]. The equilibrium

phase became pure β/B2 at 1006 ºC, above which the phase constituent remained unchanged in the Ti-Al-Nb system. Sintering in the single-phase region was beneficial to the homogenization of the alloy, and a relatively high sintering temperature in this phase region accelerated the sintering process. Moreover, to guarantee the solid-state sintering, 1400 ºC was used as the sintering temperature, which was 278 ºC lower than the melting point of Ti. The dependence of the diffusion to time is explained by $r=2.4(Dt)^{1/2}$ [31], where r is the radial distance, D is the diffusion coefficient, and t is the sintering time. Considering the adequate diffusion of Nb in the Ti particles, r=22.5 μm and D=9.82 $m^2 \cdot s^{-1}$ (1400 ºC) were used in this study [32], and the sintering time was calculated to be 2.5 h at a minimum. For adequate sintering, we extended the holding time to four hours.

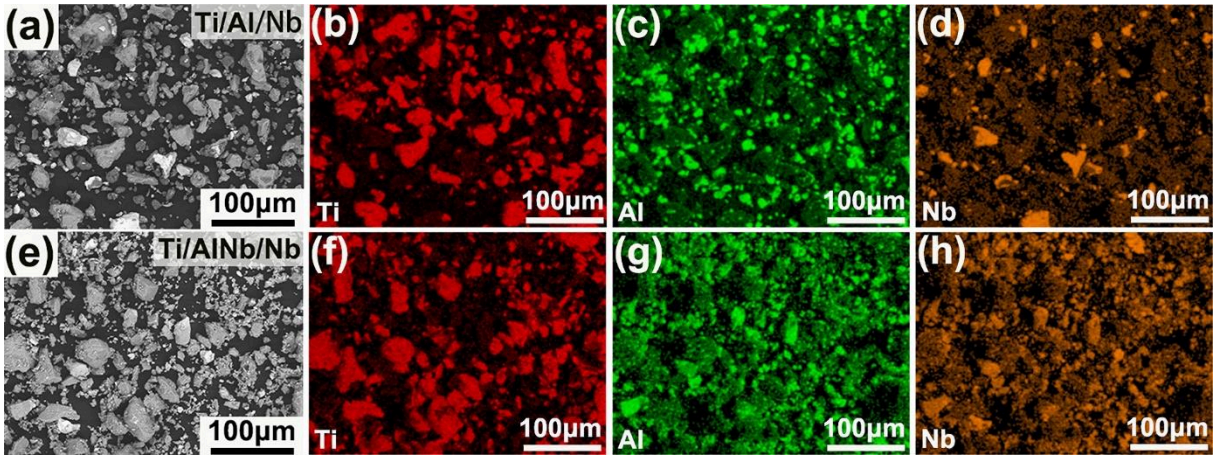

Fig. 1 (a) SEM image and (b)-(d) element mappings of the ball milled Ti/Al/Nb powders, (e) SEM image and (f)-(h) element mappings of the ball milled Ti/Al-Nb/Nb powders.

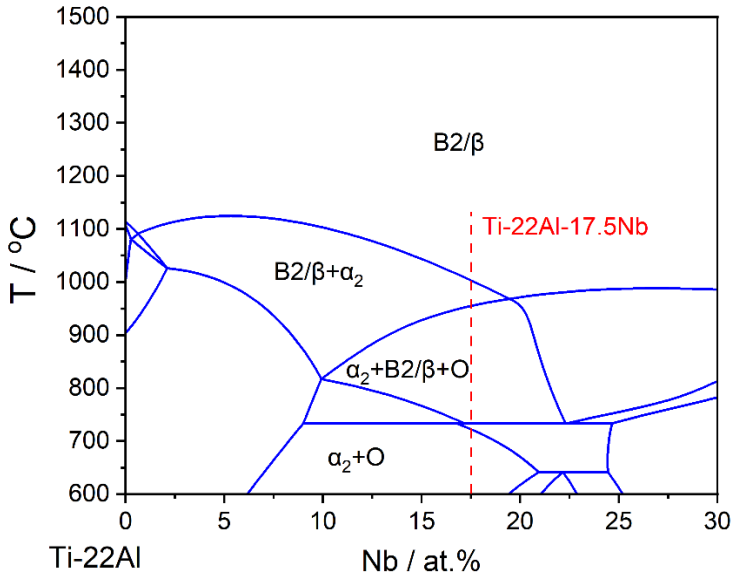

Fig. 2 Ti-22Al isopleth overlaid for an Nb composition of 17.5 at.%. Data from Cupid et al. [30].

The density of the alloys was measured by the Archimedes drainage method. The phase composition was examined by X-ray diffraction (XRD, Bruker D8 Advance), and the Rietveld refinement was performed using Fullprof Suite. The microstructure was observed by scanning electron microscope (SEM, GeminiSEM 300) and transmission electron microscope (TEM, FEI Tecnai G2 F20) equipped with energy dispersive spectroscopy (EDS, Bruker XFlash 5030). The samples for TEM observation were prepared by a focused ion beam (FIB, FEI Helios G4). The sintered alloys were subjected to quasi-static tensile tests on a universal electronic tester (CMT4305). The testing temperatures were 20 ºC and 600 °C, and the strain rate was $10^{-3}\cdot s^{-1}$.

The densification mechanism was investigated by thermal analysis and isothermal quenching experiments. The compacts were heated up to 1200 ºC in a differential scanning calorimeter (DSC, Netzsch DSC 404F3) at a heating rate of 10 ºC·min^{-1}, and the DSC curves were synchronously recorded. According to the temperatures of the exothermal and endothermal peaks, quenching temperatures were selected between 500 ºC and 1200 ºC. The compacts were sealed in vacuum quartz tubes and quenched at these temperatures to preserve the high-temperature states. The phase

composition, microstructure, and element distributions of these quenched compacts were measured by XRD, SEM, and EDS, respectively.

3. Results and discussion

3.1 Improvement of density and strength for Ti-Al-Nb alloy prepared from Al-Nb powder

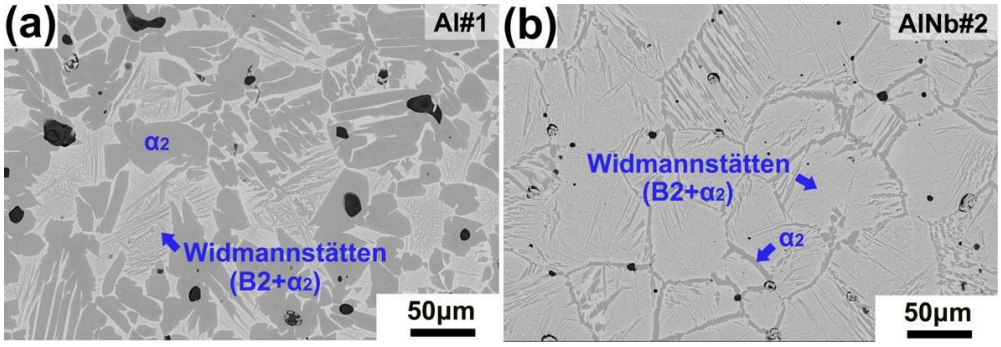

Fig. 3 Backscattered electron (BSE) images of the Ti-Al-Nb alloys prepared from (a) elemental Al powder (Al#1) and (b) Al-Nb master alloy powder (AlNb#2).

Figure 3a and b show the SEM images of the Ti-Al-Nb alloys sintered from the elemental Al powder (Al#1) and the Al-Nb master alloy powder (AlNb#2) at 1400 ºC. The Al#1 alloy contained large pores with an average diameter of 12.6±1.1 μm, and the porosity reached 3.34%. The diameter of the pores was reduced to 4.9±0.4 μm, and the porosity was decreased to 0.57% in the AlNb#2 alloy. Using the Archimedes drainage method, the densities of the Ti-Al-Nb alloys sintered from the elemental Al powder and the Al-Nb master alloy powder were measured to be 4.65 $g \cdot cm^{-3}$ and 4.98 $g \cdot cm^{-3}$, respectively. The use of the Al-Nb master alloy led to the densification of the Ti-Al-Nb alloy under the condition of pressureless sintering.

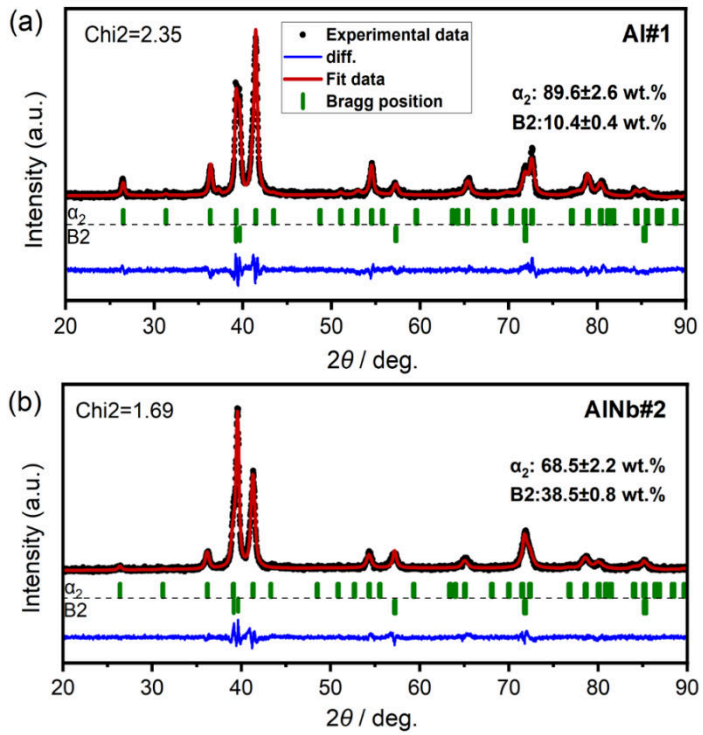

Fig. 4 XRD patterns and Rietveld refinements of the Ti-Al-Nb alloys prepared from (a) elemental Al powder (Al#1) and (b) Al-Nb master alloy powder (AlNb#2).

According to the XRD patterns (Fig. 4a and b), the phase constituent hardly changed using different raw materials, and the two alloys contained α_2 and B2 phases. The weight percentage of α_2 and B2 was calculated by the Rietveld refinement method. When using the Al-Nb master alloy powder, the content of the B2 phase in the sintered alloy was estimated to be 38.5±0.8 wt.%, which was 2.7 times larger than that in the alloy prepared from the elemental Al powder. The content of the B2 phase was also proved by the SEM images (Fig. 3a and b), in which the α_2 and B2 were dark grey and light grey, respectively. For the Ti-Al-Nb alloy prepared from the elemental Al powder (Fig. 3a), the microstructure featured equiaxed α_2 and Widmannstätten B2+α_2. The size of the equiaxed α_2 was 29.21±12.22 μm, and the width of the acicular α_2 in the Widmannstätten structure was 0.93±0.49 μm. For the Ti-Al-Nb alloy prepared from the Al-Nb master alloy powder (Fig. 3b), the microstructure featured grain-boundary α_2 and Widmannstätten B2+α_2. Compared with the equiaxed α_2 in the Al#1 alloy, the grain boundary α_2 was significantly refined in the AlNb#2 alloy, and the width was only

0.29±0.06 μm. In both alloys, the pores were located inside the α_2 phase.

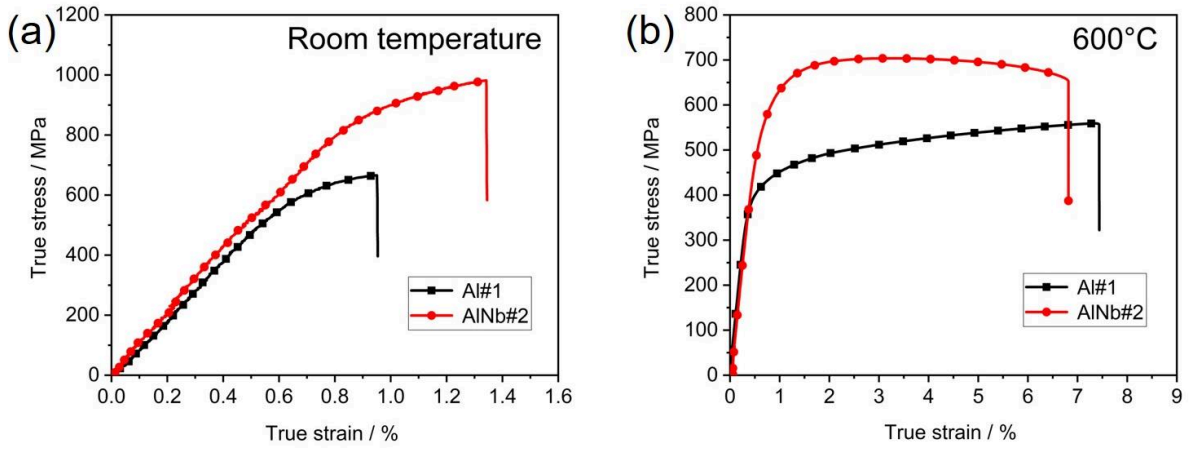

Fig. 5 True stress-strain curves of the pressurelessly sintered Ti-Al-Nb alloys at (a) room temperature and (b) 600 ºC.

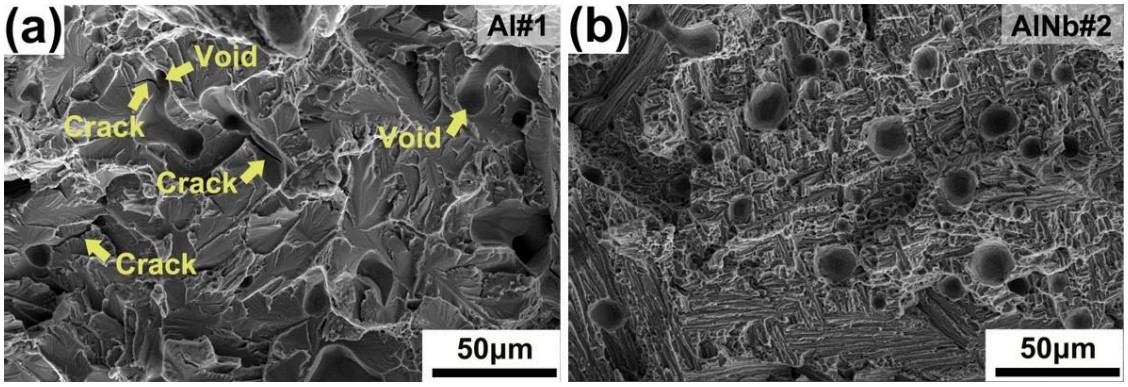

Fig. 6 Fracture morphologies of the Ti-Al-Nb alloys prepared from (a) elemental Al powder (Al#1) and (b) Al-Nb master alloy powder (AlNb#2) after room-temperature tensile tests.

The stress-strain curves of the Ti-Al-Nb alloys sintered from the elemental Al powder (Al#1) and the Al-Nb master alloy powder (AlNb#2) are shown in Fig. 5. At room temperature (Fig. 5a), the tensile strength and elongation of the Al#1 alloy were 666 MPa and 0.95%, respectively, and those of the AlNb#2 alloy was 982 MPa and 1.34%, respectively. By contrast, the tensile strength and the elongation of the AlNb#2 alloy were increased by 47% and 41%, respectively. Generally, due to a limited number of slip systems, the intermetallic α_2 phase possessed higher strength and lower ductility than the B2 phase. When the alloys were in the same composition, the reduction of the

equiaxed α_2 phase decreased the strength of the alloy, whereas the refined acicular α_2 led to substantial second-phase strengthening for the high strength of the AlNb#2 alloy. Side evidence was found in the fracture morphologies of the two alloys (Fig. 6a and b). The fracture mainly occurred at the interfaces of the α_2 and B2 phases in the Widmannstätten structure, indicating that the second phase strengthening might be the dominant mechanism for the Ti-Al-Nb alloys. Since the content of the B2 phase increased in the AlNb#2 alloy, the plasticity was improved. More importantly, the voids with a diameter of 8-18 μm were evident on the fracture surface of the Al#1 alloy, and the cracks extended from these voids. However, fewer voids or cracks were observed in the fracture surface of the AlNb#2 alloy. It indicated that the absence of the pores played an essential role in increasing the mechanical properties of the Ti-Al-Nb alloys by pressureless sintering. At 600 °C, although the elongation of the AlNb#2 alloy was 8% lower than that of the Al#1 alloy, the tensile strength of the AlNb#2 alloy (702 MPa) was 26% higher than that of the Al#1 alloy. Compared with the mechanical properties of the AlNb#2 alloy at room temperature, the tensile strength at 600 °C was only decreased by 29%, and the elongation was increased by 408%. Hence, besides the densification, the Al-Nb alloy powder also benefited the elevated-temperature mechanical properties.

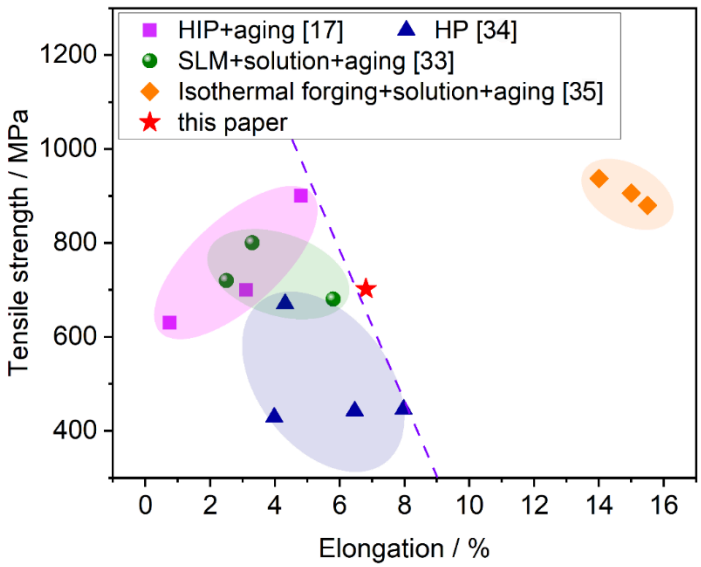

Fig. 7 Tensile strength and elongation of Ti_2AlNb alloys prepared by hot isostatic pressing, selective

laser melting (SLM), hot pressing (HP) sintering, forging, and pressureless sintering [17, 33-35]. A red star indicates the result of the present study.

Figure 7 shows the high-temperature (600 ºC or 650 ºC) tensile strength and the elongation of the Ti-Al-Nb alloys fabricated by hot isostatic pressing, selective laser melting (SLM), hot pressing (HP) sintering, forging, and pressureless sintering [17, 33-35]. The hot-pressed alloys only possessed relatively high plasticity, while the HIPped ones only showed high strength. Moderate strength and plasticity were achieved in the SLMed alloys. When the alloys were subjected to severe deformation and multistep heat treatment, excellent high-temperature strength and plasticity were obtained. A red star indicates the result of the present study in Fig. 7. When the complex process was undesirable, the pressurelessly sintered Ti-Al-Nb alloys were competitive in strength and plasticity at 600-650 ºC.

3.2 Phase transitions upon heating

The above analyses proved that the removal of the pores was conducive to the mechanical properties of the pressurelessly sintered Ti-Al-Nb alloys. We first studied the phase transitions in the sintering process to reveal the densification mechanism of the Ti-Al-Nb alloys prepared from Al-Nb master alloy powder. The DSC curves of the compacts upon heating are shown in Fig. 8. Two continuous exothermic peaks existed on the DSC curve for the compact of the Ti, Al, and Nb powders, and the peak temperature was 617 ℃ and 657 ℃, respectively. The two peaks originated from overlapping the exothermic peak for the reaction of $Ti+3Al \rightarrow TiAl_3$ [28] and the endothermic peak for the melting of Al. Therefore, the two peaks corresponded with the reactions of $Ti(s)+3Al(s) \rightarrow TiAl_3(s)$ and $Ti(s)+3Al(l) \rightarrow TiAl_3(s)$, respectively. By contrast, for the compacts of the Ti, Al-Nb alloy, and Nb powders, neither exothermic nor endothermic peaks appeared on the DSC curve in the temperature range of 600-700 ºC.

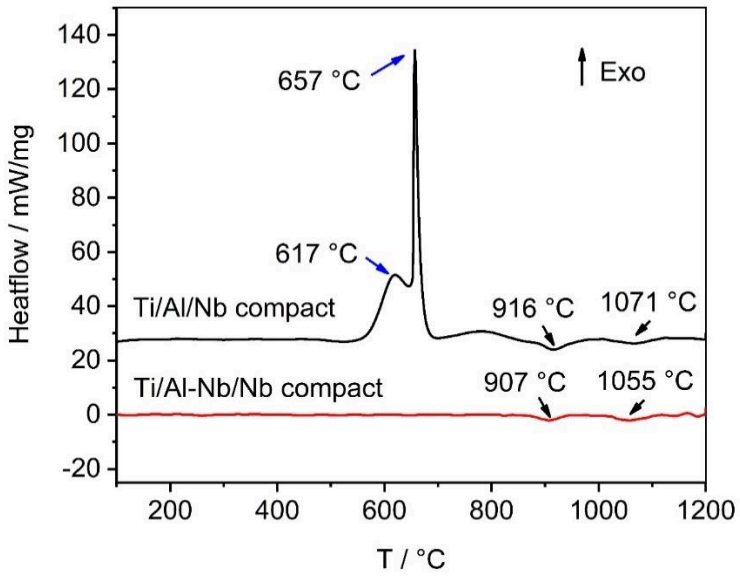

Fig. 8 DSC curves for the compacts of Ti, Al, and Nb powders and Ti, AlNb, and Nb powders.

The pores in the sintered Ti-Al-Nb alloys are strongly associated with the reaction of Ti and Al, since the transient liquid Al phase would remain pores in the alloy [36]. Since no simple substance of Al existed, the chemical reaction of Al powder and Ti powder no longer occurred during the sintering of the AlNb#2 alloy. At 900-1100 ℃, two endothermic peaks were observed on both DSC curves of the two compacts from different raw material systems. The temperatures of the two endothermic peaks, 907 ℃ and 1055 ℃, for the compact prepared from Al-Nb alloy powder are lower than those, 916 ℃ and 1071 ℃, for the compact of elemental powder, respectively. It indicated that the phase transitions of α→β and α_2→B2 occurred at lower temperatures for the AlNb#2 alloy. Although the reaction of Ti+3Al→$TiAl_3$ was avoided in the AlNb#2 alloy, the phase transition of α_2→B2 still occurred, indicating that the Ti_3Al phase might generate from the Ti and Al-Nb master alloy.

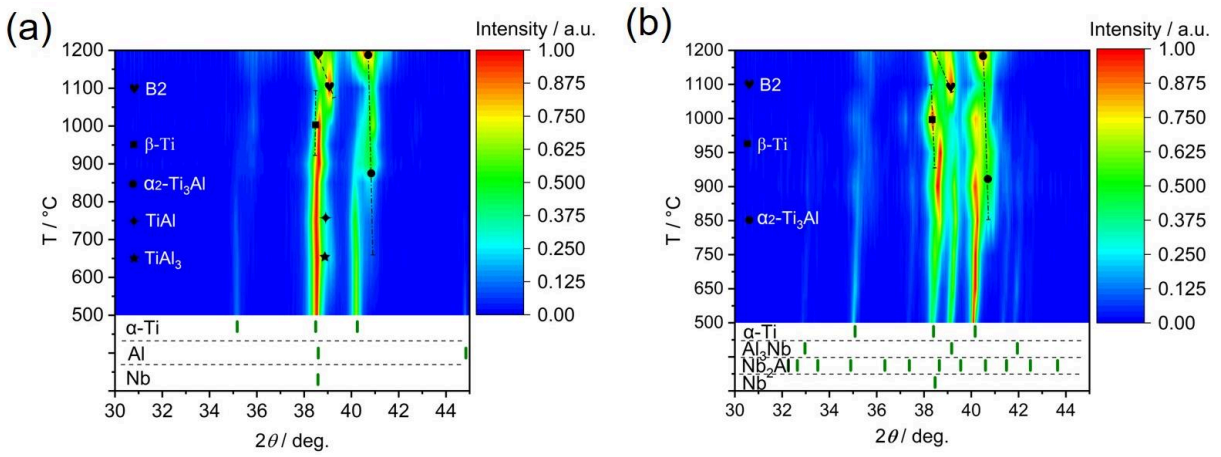

Fig. 9 XRD patterns of (a) Ti/Al/Nb and (b) Ti/Al-Nb/Nb compacts quenched at 500-1200 ºC.

The compacts were quenched at 500 °C, 650 °C, 750 °C, 850 °C, 900 °C, 950 °C, 1000 °C, 1100 °C, and 1200 °C to remain in the high-temperature states at room temperature. We identified the phase transitions upon heating by examining the phase composition and microstructure at these temperatures. The XRD patterns for the compacts of the Ti, Al, and Nb powders quenched at 500-1200 ºC are shown in Fig. 9a. Only the region of 2θ=34-42º was shown. At 500 ºC, the Ti, Al, and Nb phases were all in their original states, which were verified as hexagonal close-packed (hcp) α-Ti phase, face-centered cubic (fcc) Al phase, and body-centered cubic (bcc) Nb phase, respectively. At 650 ºC, the Al phase disappeared, and the $TiAl_3$ phase formed, corresponding to the two exothermal peaks on the DSC curve (Fig. 8). The reaction was $Ti+3Al \rightarrow TiAl_3$. At 750 ºC, the increasing peak intensity of γ-TiAl and α_2 accompanied by the decreasing peak intensity of $TiAl_3$ since the interdiffusion of Al and Ti proceeded. The reactions were $2Ti+TiAl_3 \rightarrow 3TiAl$ and $8Ti+TiAl_3 \rightarrow 3Ti_3Al$. At 850 ºC, the peak intensities of α-Ti and $TiAl_3$ significantly decreased, and the peak intensity of the α_2 phase increased. The reaction was mainly $8Ti+TiAl_3 \rightarrow 3Ti_3Al$. At 900 °C, the peaks of the γ-TiAl phase disappeared, and the peak intensity of the α_2 phase further increased. The reaction was $2Ti+TiAl \rightarrow Ti_3Al$. Meanwhile, the α-Ti transformed into the β-Ti, which was consistent with the endothermal peak (916 ºC) on the DSC curve for the compact of the Ti, Al, and Nb powders. At 950 ºC

and 1000 °C, the peak intensity of the α_2 phase was increased. At 1100 °C, the peak intensity of Nb dropped dramatically, and the peaks of the α_2-Ti_3Al shifted towards the direction of a small angle, indicating the Nb atoms with a larger atomic radius than the Ti atoms were incorporated in the Ti_3Al lattice. With the increasing Nb concentration, the Ti_3Al phase transformed into the B2 phase, which was identified as the main phase in the XRD pattern. This phase transition corresponded to the endothermal peak (1071 °C) on the DSC curve of the Ti, Al, and Nb powders. At 1200 °C, the diffusion of Nb was accelerated, promoting the phase transition of $\alpha_2 \rightarrow$B2 and the homogenization of the composition. However, the XRD pattern showed that the α_2 phase was the main phase at 1200 °C. It was due to the quenching-induced B2$\rightarrow\alpha_2$ phase transformation when the compact was cooled down to room temperature.

The XRD patterns of the Ti/Al-Nb/Nb compacts quenched at 500-1200 °C are shown in Fig. 9b. Below 750 °C, the Ti, Al-Nb (Al_3Nb and $AlNb_2$), and Nb phases were in their original states. At 850 °C, the peak intensity of the $NbAl_3$ phase decreased, and that of the Nb_2Al and α_2 phases increased. The reaction was $2NbAl_3+15Ti \rightarrow 5Ti_3Al+Nb_2Al$. At 900 °C, the α-Ti transformed into β-Ti, corresponding to the endothermal peak (907 °C) on the DSC curve of the Ti/AlNb/Nb compact. At 950 °C, the peaks of the $NbAl_3$ and Nb_2Al phases decreased, while that of the α_2 phase increased. Moreover, the peak position of the α_2 phase shifted towards the direction of a small angle, indicating that the formed α_2 lattices might contain a certain number of Nb atoms. The temperature for this peak shift was 150 °C lower than that in the compact of the Ti, Al, and Nb powders. The reaction was $Nb_2Al+3Ti \rightarrow Ti_3Al+2Nb$. At 1000 °C, the released Nb accelerated the phase transformation of $\alpha \rightarrow \beta$, and the peak of the β-Ti phase at 2θ=38.3° was increased. At 1100 °C, the Ti, Al-Nb, and Nb phases were entirely consumed, and the α_2 phase transformed into the B2 phase, corresponding to the

endothermal peak (1055 ºC) on the DSC curve for the Ti/Al-Nb/Nb compact. At 1200 ºC, the phase transformation and the homogenization processes were similar to those in the Ti/Al/Nb compacts.

According to the XRD patterns, the phase transitions of the two compacts upon heating were summarized as follows. The compact of the Ti, Al, and Nb powders experienced the phase transitions of α-Ti+Al→$TiAl_3$→γ-TiAl→α_2-Ti_3Al, α-Ti→β-Ti, and α_2→B2 upon heating. The compact of the Ti, Al-Nb, and Nb powders experienced α-Ti+Al_3Nb→α_2-Ti_3Al+Nb_2Al, Nb_2Al+3Ti→Ti_3Al+2Nb, α-Ti→β-Ti, and α_2→B2 [37, 38].

3.3 Microstructure evolution upon heating

The microstructure of the compacts at various temperatures was examined, and the microstructure evolution during the sintering processes was investigated. For the compacts of Ti, Al, and Nb powders, the SEM images of the compacts quenched at 500-1200 ºC are shown in Fig. 10. In the SEM images, the Ti, Al, and Nb particles were in grey, black, and bright white color, respectively. The corresponding EDS results are shown in Table 1.

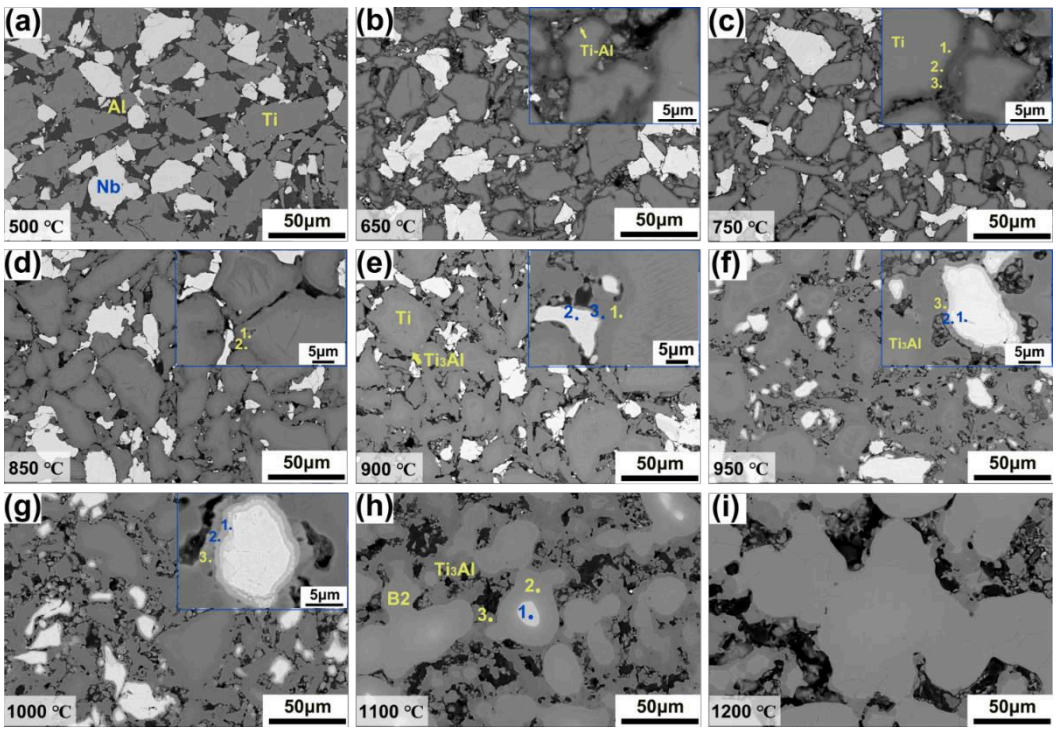

Fig. 10 BSE images of the Ti/Al/Nb compacts quenched at (a) 500 ºC, (b) 650 ºC, (c) 750 ºC, (d)

850 ºC, (e) 900 ºC, (f) 950 ºC, (g) 1000 ºC, (h) 1100 ºC, and (i) 1200 ºC.

Table 1 EDS results of the Ti/Al/Nb compacts quenched at 750 °C, 850 °C, 900 °C, 950 °C, 1000 °C, and 1100 °C.

T/ºC	Figure	Point	Ti/at.%	Al/at.%	Nb/at.%
750°C	10(c)	1	75.32	24.68	0.00
		2	51.82	48.18	0.00
		3	25.43	74.57	0.00
850°C	10(d)	1	74.25	25.75	0.00
		2	53.97	46.03	0.00
900°C	10(e)	1	74.64	25.36	0.00
		2	1.33	0.05	98.62
		3	63.30	25.22	11.49
950°C	10(f)	1	1.13	0.00	98.87
		2	26.60	20.82	52.58
		3	62.94	26.98	10.08
1000°C	10(g)	1	27.50	19.33	53.17
		2	53.42	21.52	25.06
		3	65.61	25.84	8.55
1100°C	10(h)	1	9.40	2.04	88.57
		2	61.86	19.60	18.54
		3	70.76	24.82	4.42

At 500 ℃, the Ti, Al, and Nb particles were separated from each other (Fig. 10a). According to

the XRD pattern, they remained unreacted in the compact (Fig. 9a). At 650 ℃, the Ti-Al compounds formed at the edge of the Ti particles (inset of Fig. 10b), reducing the gaps among the Ti, Al, and Nb particles. The cell volume of $TiAl_3$ and α-Ti is 509.5 Å and 35.3 Å, respectively; therefore, the formation of $TiAl_3$ resulted in a significant increase in the volume of the original Ti particles. Both the DSC curve (Fig. 8) and the XRD patterns (Fig. 9a) confirmed the phase transformation of $Ti+Al \rightarrow TiAl_3$ at this temperature. At 750 ℃, since the diffusion rate of Ti (1.5×10^{-3} $m^2\cdot s^{-1}$) is lower than that of Al (2.1×10^{1} $m^2\cdot s^{-1}$) at the Ti/Al interface [39], the $TiAl_3$, TiAl, and Ti_3Al formed from the outer to the inner layers of the Ti particles (inset of Fig. 10c). The formation sequence was $TiAl_3 \rightarrow TiAl \rightarrow Ti_3Al$, which was in agreement with the decreasing concentration of Al. At 850 ℃, the $TiAl_3$ layer disappeared, and the two layers that remained on the surface of the Ti particles were identified to be TiAl and Ti_3Al phases from the outer to the inner layers, as indicated in the inset of Fig. 10d. At 900 ℃, the TiAl phase transformed into the Ti_3Al phase, and only one Ti_3Al layer remained on the surface of the Ti particles. Sun et al. and Huang et al. also reported similar phase transformations upon sintering the Ti-Al and Ti-Al-Nb alloys [40, 41]. With the increasing temperature, the content of the Ti-Al compounds gradually increased, as the thickness of the layers on the surface of the Ti particles became larger, from 0.64 μm at 650 ℃ to 3.86 μm at 900 ℃.

Above 900 ℃, the refractory Nb began to diffuse, as the outermost Ti_3Al layer contained 11.49 at.% Nb (inset of Fig. 10e), according to the EDS results. Meanwhile, only a small amount of Ti (1.33 at.%) existed inside the Nb particles, indicating that the diffusion rate of Ti in Nb (diffusion coefficient of 2.08×10^{-21} $m^2\cdot s^{-1}$ at 920 ℃ [42]) was lower than that of Nb in Ti_3Al (diffusion coefficient of 5.56×10^{-19} $m^2\cdot s^{-1}$ at 920 ℃ [32]). Along with the Nb and Ti interdiffusion, the Ti-Al-Nb compounds were produced on the surface of the Nb particles. At 950 ℃, the two layers were confirmed to be $AlNb_3$

containing 26.60 at.% Ti and Ti_3Al containing 10.08 at.% Nb, as shown in Fig. 10f and Table 1. The $AlNb_3$ phase was not detected by the XRD. At 1000 °C, the layers were $AlNb_3$, B2, and Ti_3Al from the inner to the outer layers of the Nb particles (Fig. 10g). The layers became thicker than those at 950 °C. At 1100 °C, the diameter of the Nb particles was reduced to 14.7 μm due to the increasing diffusion rate of Nb (Fig. 8h). With the increasing Nb content in the Ti_3Al phase, the Ti_3Al transformed into B2. This transition also accorded with the endothermal peak at 1071 °C on the DSC curve of the Ti/Al/Nb compact (Fig. 8). At 1200 °C, the diffusion and the phase transition continued, and the composition of the alloy became homogeneous.

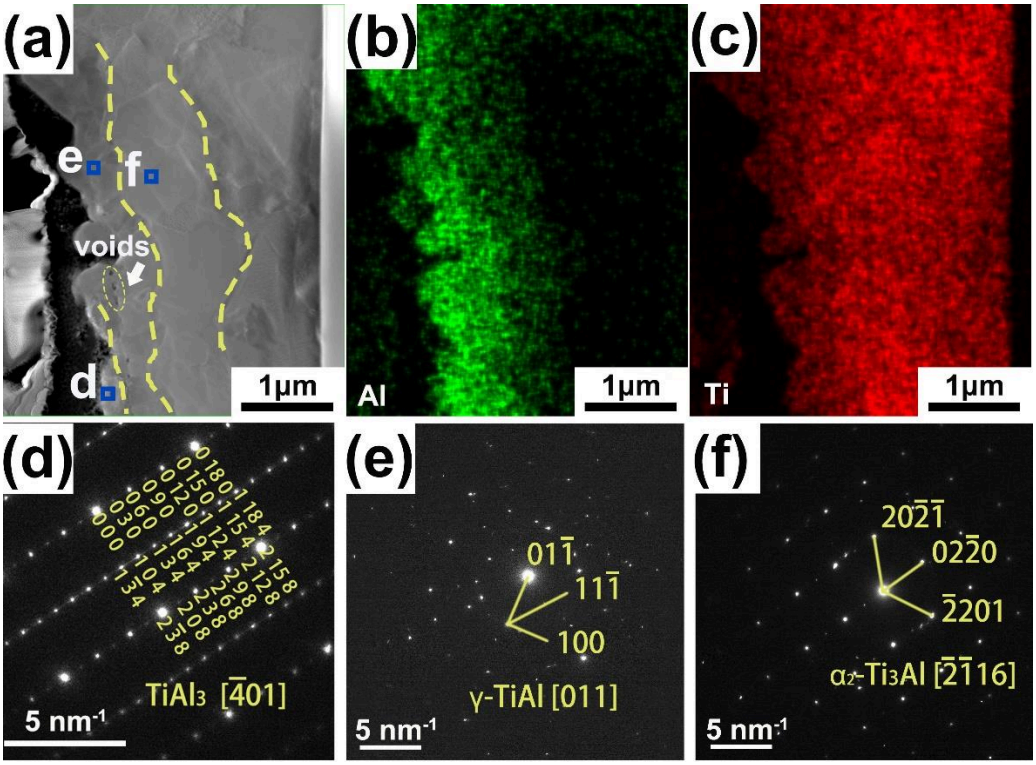

Fig. 11 (a) HADDF image, (b) and (c) element mapping of the Ti/Al/Nb compact quenched at 750 °C, and (d)-(f) SAED patterns of the corresponding regions in (a).

Combined with the XRD and SEM analyses, the phase transition sequence was re-concluded as follows. Upon heating, the compact of the Ti, Al, and Nb powders experienced the phase transitions of α-Ti+Al→$TiAl_3$→γ-TiAl→α_2-Ti_3Al, α-Ti→β-Ti, α_2→B2, Al+3Nb→$AlNb_3$ (ΔH_{cal}=-67 kJ·mol^{-1}),

and $AlNb_3$+2Ti_3Al→3Ti_2AlNb(B2) (ΔH_{cal}=-37 kJ·mol^{-1}) [38]. The transformations among the $TiAl_3$, TiAl, and Ti_3Al phases were further confirmed by the TEM, as shown in Fig. 11. In addition to the element mappings that showed the continuous concentration change of the Ti and Al (Fig. 11b and c), the selected area electron diffraction (SAED) patterns were employed to confirm the three phases. The region in the high-angle annular dark-field (HADDF) image (Fig. 11a) was divided into three layers, which were confirmed to be $TiAl_3$, TiAl, and Ti_3Al from the left to the right side (Fig. 11d-f). The $TiAl_3$ and TiAl phases were the intermediate phases for producing the Ti_3Al phase. The SAED pattern for the $TiAl_3$ phase is shown in Fig. 11d. The distance between the second brightest spot and the central spot was 4.908 nm^{-1}, and five extra spots were between the two pots, forming an 18R-type long-period stacking ordered (LPSO) structure. It was due to the interruption of the periodic repeating octahedral structure in the crystal lattice of the $TiAl_3$ phase. Six octahedral structure was stacked along the *b*-axis in a $TiAl_3$ superlattice. Overall, the compounds were $TiAl_3$, TiAl, and Ti_3Al from the outer to the inner layers of the Ti particle. Since the B2 phase contained less Al than the α_2 phase, Al was released when the phase transformation of α_2→B2 occurred. Subsequently, the $AlNb_3$ was formed from Al and Nb.

The standard Gibbs free energy (ΔG) of the mentioned phase transformations was calculated according to the thermodynamic data reported by Cupid et al. [30] and George et al. [43]. The ΔG -T curves are shown in Fig. 12. A negative ΔG value indicated that the phase transformation was spontaneous at the corresponding temperature. The more negative the ΔG, the more spontaneous the phase transformation. Therefore, the Ti-Al compounds were spontaneously formed in the temperature range of 200-1400 ºC, and the phase transformations of Al+3Nb→Nb_3Al and α_2→B2 were non-spontaneous (Fig. 12a and 12b). In addition, the phase transformation of α→β was spontaneous above

1160 °C. According to the values of ΔG, the formation sequence of the phases was $TiAl_3 \rightarrow TiAl \rightarrow Ti_3Al \rightarrow \beta \rightarrow Nb_3Al \rightarrow B2$, which agreed well with the above-concluded sequence of the phase transformations in the Ti/Al/Nb compacts.

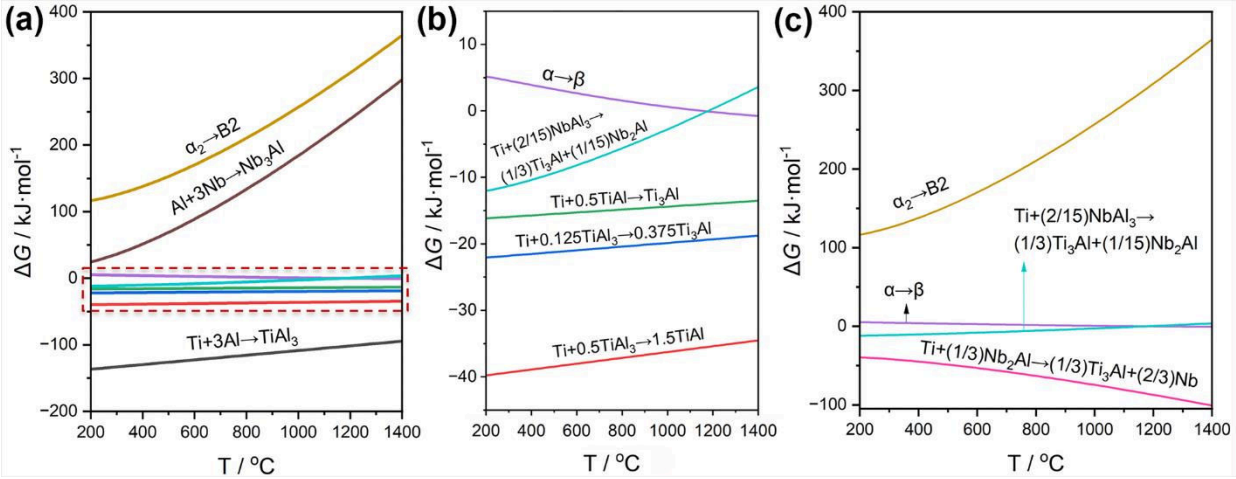

Fig. 12 Gibbs free energy (ΔG) of the concerned phase transformations (a) and (b) in the Ti/Al/Nb compacts, and (c) in the Ti/Al-Nb/Nb compacts. (b) is the enlargement of (a). Data from Cupid et al. [30] and George et al. [43].

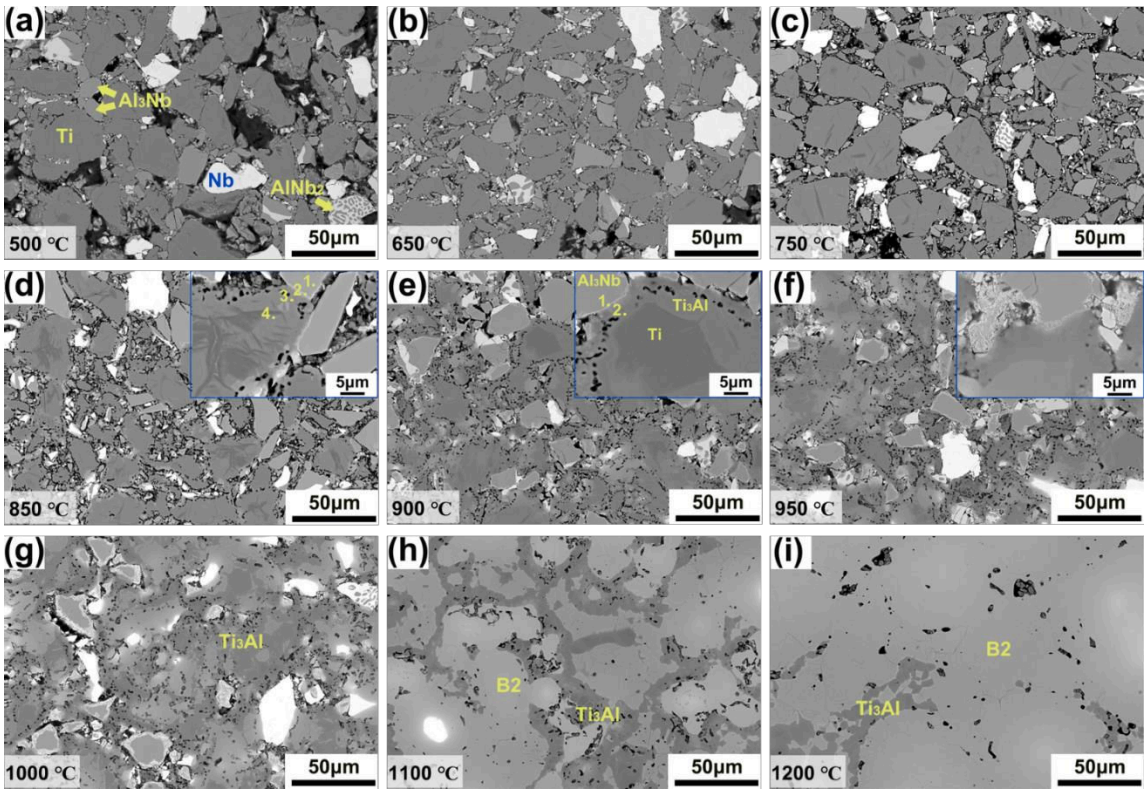

Fig. 13 BSE images of the Ti/Al-Nb/Nb compacts quenched at (a) 500 °C, (b) 650 °C, (c) 750 °C, (d) 850 °C, (e) 900 °C, (f) 950 °C, (g) 1000 °C, (h) 1100 °C, and (i) 1200 °C.

Table 2 EDS results of the Ti/Al-Nb/Nb compacts quenched at 850 °C and 900 °C.

T/ºC	Figure	Point	Ti/at.%	Al/at.%	Nb/at.%
850°C	13(d)	1	0.35	73.95	25.70
		2	17.53	34.83	47.64
		3	67.93	25.07	6.99
		4	99.73	0.27	0.00
900°C	13(e)	1	18.28	36.28	45.45
		2	71.61	23.49	4.91

For the compacts of Ti, Al-Nb, and Nb powder, the SEM images of the compacts quenched at 500-1200 ℃ are shown in Fig. 13. At 500 ºC, the Ti, Al_3Nb, $AlNb_2$, and Nb particles, which were in dark grey, light grey, cow pattern, and bright white color, respectively (Fig. 11a), were separated from each other. The XRD pattern also showed that the Ti, Al_3Nb, $AlNb_2$, and Nb phases existed in their original states at 500 ºC (Fig. 9b). At 650 ºC, the distances among the particles were reduced (Fig. 13b). The expansion of the particles with the increasing temperature might account for this phenomenon. According to the results of the XRD patterns, no phase transitions occurred at this temperature, which was different from the Ti/Al/Nb compact. At 750 ºC, the Nb and Al-Nb particles were still isolated by the connecting Ti particles (Fig. 11c). Layers were absent on the surfaces of the Nb or Ti particles. At 850 ºC, 0.35 at.% Ti was dissolved in the Al_3Nb phase, and 0.27 at.% Al was dissolved in the α-Ti phase, indicating that the interdiffusion of the Ti and Al-Nb alloy occurred (Fig. 11d). As a result, the Ti_3Al layer formed between the Ti and the Al_3Nb particles. It indicated that the reaction of $Ti+Al_3Nb \rightarrow Ti_3Al+Nb_2Al$ occurred. Specifically, 6.99 at.% Nb was dissolved in the Ti_3Al phase, and 17.53 at.% Ti was in the Nb_2Al phase. The micropores formed at the side of the Ti particles,

while the Nb_2Al layer formed at the Al_3Nb side. The layers of the Ti_3Al and Nb_2Al were 2.8 μm and 0.3 μm, respectively. At 900 ºC, the average thickness of Ti_3Al and Nb_2Al layers was increased to 5.7 μm and 0.5 μm, respectively (Fig. 13e). At 950 ºC, an increasing amount of Ti_3Al formed on the Nb particles (Fig. 13f), since the diffusion between the Ti and Al-Nb particles was accelerated by the α→β transition occurred at 907 ℃ (Fig. 8). At 1000 ºC, the Nb_2Al and Ti_3Al layers increased, and the Nb content in the Ti_3Al phase was also increased. At 1100 ºC, the Ti, Nb, and Al-Nb phases were continuously consumed to form the Ti_3Al phase, and meanwhile, the phase transformation of α_2→B2 occurred. The Ti_3Al, B2, and residual Nb regions were recognized in Fig. 13h. At 1200 ℃, most of the Ti_3Al phase transformed into the B2 phase. With the increasing amount of the B2 phase, the composition of the compact became uniform. Overall, the SEM observation was in good agreement with the XRD analyses.

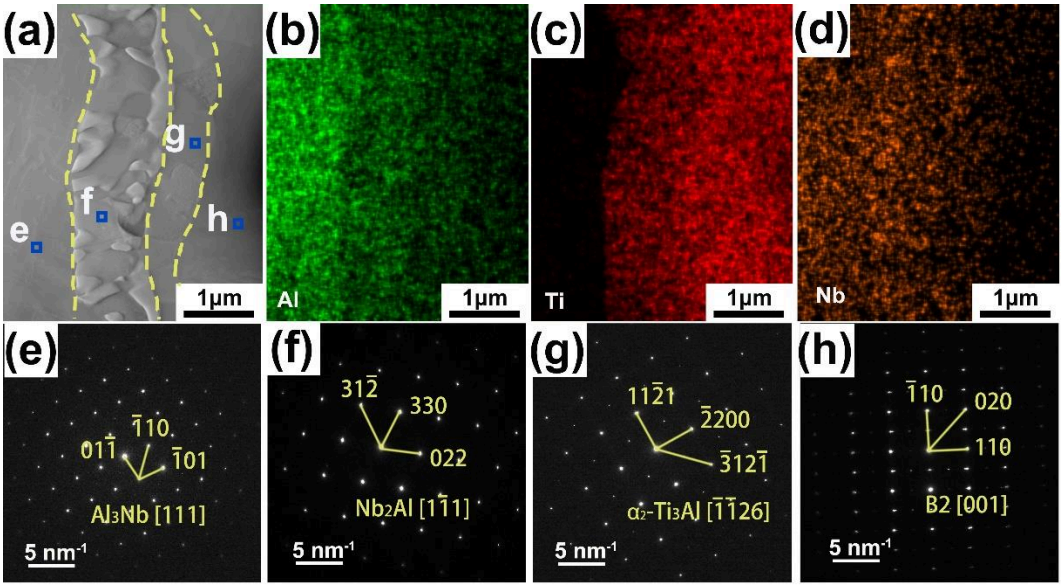

Fig. 14 (a) HADDF image, (b)-(d) element mapping of the Ti/Al/Nb compact quenched at 950 ºC, and (e)-(h) SAED patterns of the corresponding regions in (a).

The transformations among the $TiAl_3$, Nb_2Al, Al_3Nb, and B2 phases were further confirmed by the TEM, as shown in Fig. 14. In addition to the element mappings that showed the continuous

concentration change of the Ti, Al, and Nb, the selected area electron diffraction (SAED) patterns were employed to confirm the three phases. The four layers were Al_3Nb, Nb_2Al, Ti_3Al, and B2 from the left to the right side of the HADDF image. The ΔG for the concerned reactions in the Ti/Al-Nb/Nb compacts is shown in Fig. 12c. The phase transformation of $Nb_2Al+3Ti \rightarrow Ti_3Al+2Nb$ was spontaneous in the temperature range of 200-1400 ºC, and that of $2NbAl_3+15Ti \rightarrow Nb_2Al+5Ti_3Al$ was spontaneous below 1180 ºC. Therefore, the formation sequence was confirmed to be $Ti_3Al \rightarrow \beta \rightarrow B2$, which agreed well with the XRD and SEM analyses in the Ti/Al-Nb/Nb compacts.

3.4 Densification mechanism

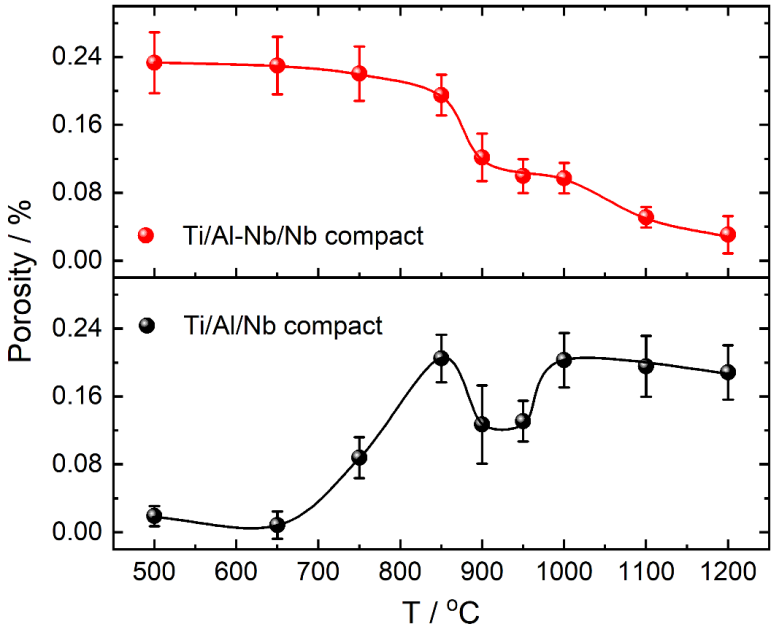

Fig. 15 Porosity of the Ti/Al/Nb and Ti/Al-Nb/Nb compacts quenched at 500-1200 ºC.

Comparing the SEM images of the Ti/Al/Nb and Ti/Al-Nb/Nb compacts sintered at 1200 ºC (Figs. 10i and 13i), the Ti/Al-Nb/Nb compact contained fewer pores. The porosity of the Ti/Al/Nb and Ti/Al-Nb/Nb compacts was 18.83% and 3.07% at 1200 ºC, respectively. It proved that using the Al-Nb master alloy was beneficial to the densification of the Ti-Al-Nb alloys in the condition of pressureless sintering. The densification of the Ti/Al/Nb and Ti/Al-Nb/Nb compacts during the sintering process was clarified by illustrating the porosity of the compacts at 500-1200 ºC (Fig. 13).

For the Ti/Al/Nb compact, two sharp increases were found on the curve at 650 ºC and 950 ºC, respectively. Combined with the DSC, XRD, and SEM analyses, the critical phase transitions that affected the density of the compacts were figured out, and a schematic diagram of the sintering process is shown in Fig. 16a. When the Ti, Al, and Nb powders were used as the raw materials, the powders were pressed into a dense green compact, since the soft Al filled the spaces among the Ti and Nb particles. This accounted for the low porosity of the Ti/Al/Nb compacts at 500 ºC and 650 ºC. The Al powder was wrapped on the surface of the Ti powder until melting. As the temperature increased, the $TiAl_3$ phase was rapidly produced at the surface of the Ti particles. The transient liquid Al phase was the reason for the sharp increase of the porosity at 650 ºC, and the pores remained in the regions of the original Al particles. In the temperature range of 650-850 ºC, the phase transitions of $TiAl_3 \rightarrow TiAl \rightarrow Ti_3Al$ proceeded, which was strongly dependent on the diffusion of Al and Ti. The difference in the diffusion rate of Al in Ti and Ti in Al led to micro Kirkendall pores in the Ti-Al intermetallic compounds (Fig. 8b-d and 9a), and the porosity of the compact increased. This also accorded with the phenomenon that the pores were located inside the α_2 phase in the sintered alloys (Fig. 1). At 900 ºC, an increasing amount of Ti_3Al phase formed rapidly from the TiAl phase or the α-Ti. The theoretical cell volumes of the α-Ti, TiAl, and Ti_3Al are 35.22 $Å^3$, 64.01 $Å^3$, and 133.96 $Å^3$, respectively [44-46]. The formation of the Ti_3Al phase led to the expansion of the TiAl-coated Ti particles, reducing the porosity. When the heating temperature exceeded 900 ºC, the interdiffusion among the Ti, Al, and Nb initiated in the α_2 and Nb phases, forming the Nb-contained α_2 phase and the Ti-contained $AlNb_3$ phase at the surface of the Ti and Nb particles, respectively. Since the diffusion coefficient of Al in Nb (1.48×10^{-15} $cm\cdot s^{-1}$ at 1060 ºC [47]) is larger than that of Nb in Ti_3Al (7.55×10^{-21} $cm\cdot s^{-1}$ at 1060 ºC [32]), the strong Kirkendall effect led to the formation of the pores at the side of

the Ti_3Al phase. Therefore, the porosity of the compact increased in the temperature range of 900-1000 °C. The pores that originated from the Kirkendall effect were closed in the following homogenization stage. At 1000-1200 °C, the α_2 phase with the theoretical cell volume of 133.96 $Å^3$ transformed into the B2 phase with that of 33.79 $Å^3$. Nevertheless, the ripening of the B2 phase offset the volume reduction, and the overall porosity of the compact was decreased.

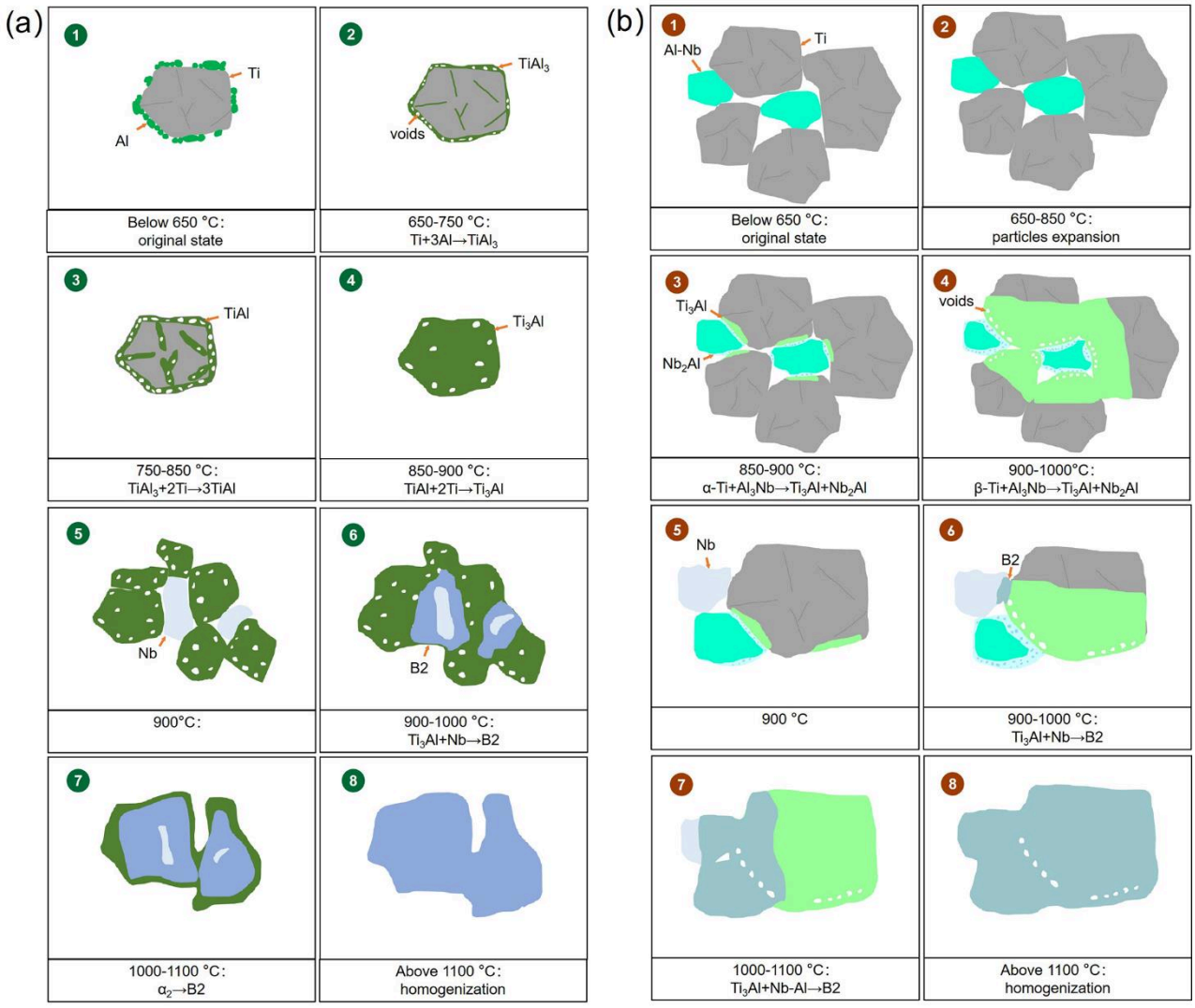

Fig. 16 Schematic diagrams of the sintering processes of (a) Ti/Al/Nb compact and (b) Ti/Al-Nb/Nb compact.

The porosity of the Ti/Al-Nb/Nb compact decreased continuously in the temperature range of 500-1200 °C (Fig. 15). The schematic diagram of the sintering process is shown in Fig. 16b. Since the Al-Nb master alloy was not as soft as the Al powder, the porosity of the Ti/Al-Nb/Nb green

compact was larger than that of the Ti/Al/Nb one below the melting point of Al. Nevertheless, the expansion of the Ti and Al-Nb particles with the increasing temperature decreased the porosity, and the particles became connecting at 650 ºC. Since no melting of Al occurred in this system, the porosity was gently decreased until 850 ºC, which was different from the Ti/Al/Nb compact. At 850 ºC, the reaction of α-Ti+3Al→α_2-Ti_3Al led to the expansion of the Ti particles and the reduction of the porosity. However, the interdiffusion occurred at the interfaces of the Ti_3Al-coated Ti particles and the Al-Nb master alloy particles. The Kirkendall effect resulted in minor pores at the Ti_3Al side, since the diffusion rate of Ti in Al_3Nb was larger than that of Al/Al_3Nb in Ti. Therefore, the phase transformation of Ti+3Al→Ti_3Al was the dominant process that reduced the porosity of the compact at this temperature. At 900 ºC, the α_2 phase became the main product after the sufficient interdiffusion between Ti and Al. The theoretical cell volumes of the α-Ti, α_2-Ti_3Al, Al_3Nb, and Nb_2Al are 35.22 $Å^3$, 127.02 $Å^3$, 139.31 $Å^3$, and 512.70 $Å^3$, respectively [48, 49]. The phase transformation of Ti+Al_3Nb→Ti_3Al+Nb_2Al led to the expansion of the particles and thus the sharp decrease of the porosity. At 950 ºC, an increasing amount of the Ti_3Al phases formed, further reducing the porosity of the compact. At 1000 ºC and 1100 ºC, the intense generation of the Ti_3Al phase and the ripening of the B2 phase should be responsible for the reduction of the porosity, respectively. Moreover, the pores originating from the Kirkendall effect were removed as the homogenization proceeded.

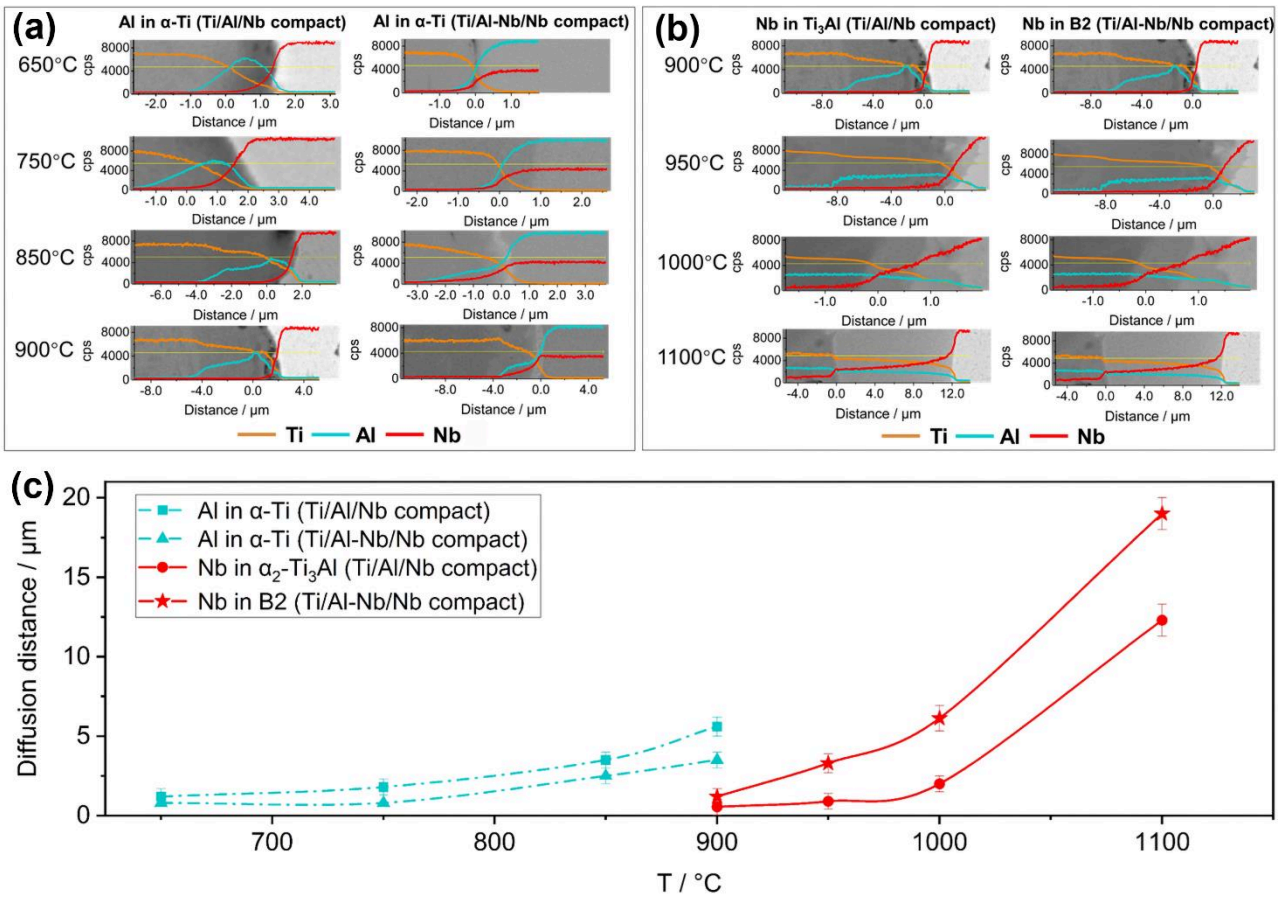

Fig. 17 EDS patterns at the interfaces of (a) Ti and Al, and (b) Nb and Ti_3Al/B2 for the Ti/Al/Nb and Ti/Al-Nb/Nb compacts quenched at 650-1100 ºC. (c) Measured diffusion distance of Al in Al in α-Ti, Nb in α_2-Ti_3Al, and Nb in B2.

The densification process was linked to the key phase transformations during the sintering process. Besides, the Kirkendall effect played an important role in affecting the porosity of the compacts. In the following text, the densification mechanism was interpreted from the viewpoint of diffusion. According to the above analyses, the diffusion of the Nb atoms initiated at 900 ºC, below which it was mainly the diffusion of the Al atoms. Therefore, the sintering process associated with the diffusion was divided into two stages, i.e. 500-900 ºC and 900-1200 ºC. The concentration of the elements in each phase was detected by EDS for the Ti/Al/Nb and Ti/Al-Nb/Nb compacts quenched at 500-1200 ºC. The diffusion rate was judged by the diffusion distances of the Al or Nb atoms away from the interfaces of two contacted particles. The results are shown in Fig. 17. To standardize the

comparison at different temperatures, the diffusion distance of the Al was measured from cps (counts per second) = 4000 to cps = 0 on the EDS pattern, and the diffusion distance of the Nb was measured from cps = 8000 to cps = 2500.

The formation of the pores was strongly associated with the rapid reaction of liquid Al with Ti in the Ti/Al/Nb compact and the faster diffusion of Al than Ti during the formation of the Ti-Al compounds. The determining factor for the densification was the growth of B2, which depended on the diffusion of Nb. Since the Al-Al metallic bond was easier to break than the Al-Nb covalent bond, the diffusion of Al in α-Ti for the Ti/Al/Nb compact was faster than that for the Ti/Al-Nb/Nb compact in the temperature range of 500-900 ºC (Fig. 17c). This was also proved by the high melting points of Al_3Nb (1680 ºC) and $AlNb_2$ (1940 ºC) [50]. When the Al powder was replaced by AlNb master alloy powder, the pores due to the melting of Al were avoided. Moreover, the diffusion rate of the Al in Al-Nb alloy was lower than that of the Al in pure Al. The Kirkendall effect between the diffusion of Ti and Al was depressed during the formation of the Ti-Al compounds; therefore, the micro Kirkendall pores were reduced in the Ti/Al-Nb/Nb compact. The formation energy of the reactions of $3Ti+Al \rightarrow Ti_3Al$ and $3Ti+(2/5)NbAl_3 \rightarrow Ti_3Al+(1/5)Nb_2Al$ was calculated to be -108 $kJ \cdot mol^{-1}$ and -58.6 $kJ \cdot mol^{-1}$ [38], indicating the former reaction could proceed at a lower temperature. The phase transformation of $Nb_2Al+3Ti \rightarrow Ti_3Al+2Nb$ was spontaneous in the temperature range of 200-1400 ºC. Since the released Nb from Nb_2Al was more active than the simple substance Nb, the diffusion of Nb in the Ti/Al-Nb/Nb compact was faster than that in the Ti/Al/Nb compact in the temperature range of 900-1100 ºC (Fig. 15c). When the AlNb master alloy was used to partially replace the Nb powder, the Kirkendall pores due to the difference in the diffusion rate of Ti and Nb were avoided. The diffusion of Nb in Ti_3Al is dominated by the vacancy mechanism [51]. During the diffusion

process, Nb occupied the position of Ti and replaced the vacancy in the sublattice of Ti_3Al [52, 53]. Therefore, the increasing diffusion rate of Nb led to the rapid densification of the Ti-Al-Nb alloy prepared from the Al-Nb master alloy powder.

4. Conclusions

In summary, a dense Ti-Al-Nb alloy was fabricated from the Al-Nb master alloy powder by cold isostatic pressing and pressureless sintering in this study. The room-temperature and high-temperature tensile strength was improved, compared with that of the alloy prepared from pure Al powder. The improvement was attributed to the removal of the pores and the refinement of the acicular α_2 phase. By comparing the phase transitions and element diffusion in the Ti/Al/Nb and Ti/Al-Nb/Nb compacts upon sintering, the densification mechanism was elucidated. In the Ti/Al/Nb compact, the sintered pores were due to the rapid consumption of liquid Al and the Kirkendall effect at the Ti_3Al/Nb interfaces, which occurred during the phase transformations of $Ti+3Al \rightarrow TiAl_3$ and $\alpha_2 \rightarrow B2$, respectively. When the elemental Al powder was replaced with the Al-Nb alloy powder, the Ti_3Al formed following the reactions of $\alpha\text{-}Ti+Al_3Nb \rightarrow \alpha_2\text{-}Ti_3Al+Nb_2Al$ and $Nb_2Al+3Ti \rightarrow Ti_3Al+2Nb$. The densification was by virtue of the decreased diffusion rate of the Al and the increased diffusion rate of the Nb, which significantly reduced the Kirkendall pores at the Ti/$AlNb_3$ and the Ti_3Al/Nb interfaces, respectively. The increased diffusion rate of Nb also accelerated the formation and ripening of the B2 phase, which also promoted the densification of the Ti-Al-Nb alloy prepared from the Al-Nb master alloy powder.

Data Availability

The raw/processed data required to reproduce these findings cannot be shared at this time due to

technical or time limitations.

Acknowledgements

This work was supported by the National Natural Science Foundation of China (grant number 52171027) and the Beijing Institute of Technology Research Fund Program for Young Scholars (grant number 202008002).

References

[1] M. Peters, J. Kumpfert, C.H. Ward, C. Leyens, Titanium alloys for aerospace applications, Adv. Eng. Mater. 5(6) (2003) 419-427.

[2] J.C. Williams, E.A. Starke, Progress in structural materials for aerospace systems, Acta Metall. 51(19) (2003) 5775-5799.

[3] M. Asta, D. de Fontaine, M. Van Schilfgaarde, First-principles study of phase stability of Ti–Al intermetallic compounds, J. Mater. Res. 8(10) (1993) 2554-2568.

[4] H.A. Lipsitt, D. Shechtman, R.E. Schafrik, The deformation and fracture of Ti_3Al at elevated temperatures, Metall. Trans. A 11(8) (1980) 1369-1375.

[5] J.B. McAndrew, Investigation of the Ti-Al-Cb system as a source of alloys for use at 12000-18000F, Wright Air Dev. Div., Air Res. Dev. Command, US Air Force 1960.

[6] A. Gogia, T. Nandy, D. Banerjee, T. Carisey, J. Strudel, J. Franchet, Microstructure and mechanical properties of orthorhombic alloys in the Ti-Al-Nb system, Intermetallics 6(7-8) (1998) 741-748.

[7] D. Banerjee, A. Gogia, T. Nandi, V. Joshi, A new ordered orthorhombic phase in a Ti_3Al-Nb alloy, Acta Metall. 36(4) (1988) 871-882.

[8] H. Zhang, N. Yan, H. Liang, Y. Liu, Phase transformation and microstructure control of Ti_2AlNb-

based alloys: a review, J. Mater. Sci. Technol. 80 (2021) 203-216.

[9] Y. Zhou, D. Wang, L. Song, A. Mukhtar, D. Huang, C. Yang, M. Yan, Effect of heat treatments on the microstructure and mechanical properties of Ti_2AlNb intermetallic fabricated by selective laser melting, Mater. Sci. Eng. A 817 (2021) 141352.

[10] S. Wang, W. Xu, B. Shao, G. Yang, Y. Zong, W. Sun, Z. Yang, D. Shan, Process design and microstructure-property evolution during shear spinning of Ti_2AlNb-based alloy, J. Mater. Sci. Technol. 101 (2022) 1-17.

[11] Q. Cai, M. Li, Y. Zhang, Y. Liu, Z. Ma, C. Li, H. Li, Precipitation behavior of Widmanstätten O phase associated with interface in aged Ti2AlNb-based alloys, Mater. Charact. 145 (2018) 413-422.

[12] Y. Zhang, Q. Cai, Y. Liu, Formation of diverse B2+O structure and hardness of Mo-modified Ti-22Al-25Nb alloys upon cooling, Vacuum 165 (2019) 199-206.

[13] M. Li, Q. Cai, Y. Liu, Z. Ma, Z. Wang, Microstructure and mechanical properties of Ti_2AlNb‐based alloys synthesized by spark plasma sintering from pre-alloyed and ball-milled powder, Adv. Eng. Mater. 20(4) (2018) 1700659.

[14] I. Polozov, V. Sufiiarov, A. Kantyukov, A. Popovich, Selective laser melting of Ti_2AlNb-based intermetallic alloy using elemental powders: Effect of process parameters and post-treatment on microstructure, composition, and properties, Intermetallics 112 (2019) 106554.

[15] H.Z. Niu, Y.F. Chen, D.L. Zhang, Y.S. Zhang, J.W. Lu, W. Zhang, P.X. Zhang, Fabrication of a powder metallurgy Ti_2AlNb-based alloy by spark plasma sintering and associated microstructure optimization, Mater. Des. 89 (2016) 823-829.

[16] L. Zhu, Y. Pan, Y. Liu, X. Wang, X. Mo, Z. Sun, H. Nan, X. Qu, X. Lu, Micro-mechanism and

mechanical properties of solid-powder hot isostatic pressing diffusion-bonded Ti_2AlNb alloy, Adv. Powder Technol. 32(10) (2021) 3610-3623.

[17] Y. Zhang, Y. Liu, L. Yu, H. Liang, Y. Huang, Z. Ma, Microstructures and tensile properties of Ti_2AlNb and Mo-modified Ti_2AlNb alloys fabricated by hot isostatic pressing, Mater. Sci. Eng. A 776 (2020) 139043.

[18] G. Wang, X. Sui, Q. Liu, Y. Liu, Fabricating Ti_2AlNb sheet with high tensile strength and good ductility by hot packed rolling the spark plasma sintered pre-alloyed powder, Mater. Sci. Eng. A 801 (2021) 140392.

[19] Z.G. Lu, J. Wu, L. Xu, X.X. Cui, R. Yang, Ring rolling forming and properties of Ti_2AlNb special shaped ring prepared by powder metallurgy, Acta Metall. Sin. 55(6) (2019) 729-740.

[20] K.H. Sim, G. Wang, J.M. Ju, J. Yang, X. Li, Microstructure and mechanical properties of a Ti−22Al−25Nb alloy fabricated from elemental powders by mechanical alloying and spark plasma sintering, J. Alloys Compd. 704 (2017) 425-433.

[21] N. Zhang, X. Han, D. Sun, S. Liu, H. Liu, W. Yang, G. Wu, Microstructure evolution and mechanical properties of LaB_6-modified Ti_2AlNb alloy fabricated by blended elemental powder metallurgy, Powder Technol. 369 (2020) 334-344.

[22] G.X. Wang, M. Dahms, Reactive powder processing of intermetallic alloys based on γ-TiAl, Structural Intermetallics (1993) 215-222.

[23] K.S. Senkevich, O.Z. Pozhoga, M.M. Serov, Features of structure formation in sintered Ti_2AlNb-based alloy produced by cold compaction and pressureless sintering, J. Phys.: Conf. Ser. 2059(1) (2021) 012019.

[24] C. Zhang, B. Lu, H. Wang, Z. Guo, V. Paley, A.A. Volinsky, Vacuum pressureless sintering of

Ti-6Al-4V alloy with full densification and forged-like mechanical properties, J. Mater. Eng. Perform. 27(1) (2018) 282-292.

[25] S.H. Kayani, N.-K. Park, Effect of Cr and Nb on the phase transformation and pore formation of Ti-Al base alloys, J. Alloys Compd. 708 (2017) 308-315.

[26] T. Chen, C. Yang, Z. Liu, H. Ma, L. Kang, Z. Wang, W. Zhang, D. Li, N. Li, Y. Li, Revealing dehydrogenation effect and resultant densification mechanism during pressureless sintering of TiH2 powder, J. Alloys Compd. 873 (2021) 159792.

[27] D. Zhao, K. Chang, T. Ebel, H. Nie, R. Willumeit, F. Pyczak, Sintering behavior and mechanical properties of a metal injection molded Ti–Nb binary alloy as biomaterial, J. Alloys Compd. 640 (2015) 393-400.

[28] Y. Liang, F. Yang, L. Zhang, J. Lin, S. Shang, Z.-K. Liu, Reaction behavior and pore formation mechanism of TiAl–Nb porous alloys prepared by elemental powder metallurgy, Intermetallics 44 (2014) 1-7.

[29] H. Wang, C. Zhang, F. Yang, P. Cao, Z. Guo, B. Lu, C. Chen, P. Liu, A.A. Volinsky, High-density and low-interstitial Ti-23Al-17Nb prepared by vacuum pressureless sintering from blended elemental powders, Vacuum 164 (2019) 62-65.

[30] D.M. Cupid, O. Fabrichnaya, O. Rios, F. Ebrahimi, H.J. Seifert, Thermodynamic re-assessment of the Ti–Al–Nb system, Int. J. Mater. Res. 100(2) (2009) 218-233.

[31] Porter D A, Easterling K E. Phase Transformations in Metals and Alloys, Agneta Engfors, 1980.

[32] J. Breuer, T. Wilger, M. Friesel, C. Herzig, Interstitial and substitutional diffusion of metallic solutes in Ti_3Al, Intermetallics 7(3-4) (1999) 381-388.

[33] X. Yang, B. Zhang, Q. Bai, G. Xie, Correlation of microstructure and mechanical properties of Ti_2AlNb manufactured by SLM and heat treatment, Intermetallics 139 (2021) 107367.

[34] J. Jia, K. Zhang, S. Jiang, Microstructure and mechanical properties of Ti–22Al–25Nb alloy fabricated by vacuum hot pressing sintering, Mater. Sci. Eng. A 616 (2014) 93-98.

[35] W. Wei, Z. Weidong, X. Chen, L. Xiaobo, Z. Jianwei, Designed bimodal size lamellar O microstructures in Ti_2AlNb based alloy: Microstructural evolution, tensile and creep properties, Mater. Sci. Eng. A 618 (2014) 288-294.

[36] P. Novák, J. Šerák, D. Vojtěch, J. Kubásek, A. Michalcová, Where reactive sintering beats melt technology, Met. Powder Rep. 63(11) (2008) 20-23.

[37] W.D. Richards, L.J. Miara, Y. Wang, J.C. Kim, G. Ceder, Interface stability in solid-state batteries, Chem. Mater. 28(1) (2016) 266-273.

[38] A. Jain, G. Hautier, S.P. Ong, C.J. Moore, C.C. Fischer, K.A. Persson, G. Ceder, Formation enthalpies by mixing GGA and GGA+ U calculations, Phys. Rev. B 84(4) (2011) 045115.

[39] E. Gamsjäger, Y. Liu, M. Rester, P. Puschnig, C. Draxl, H. Clemens, G. Dehm, F.D. Fischer, Diffusive and massive phase transformations in Ti–Al–Nb alloys–Modelling and experiments, Intermetallics 38 (2013) 126-138.

[40] Y. Sun, S.K. Vajpai, K. Ameyama, C. Ma, Fabrication of multilayered Ti–Al intermetallics by spark plasma sintering, J. Alloys Compd. 585 (2014) 734-740.

[41] X.-M. Huang, S.-X. Zhang, G.-M. Cai, H.-S. Liu, Study on the evolution of phase relations in the Ti–Al–Nb/Cr systems at 0–50 at.% Al region, Calphad 79 (2022) 102461.

[42] Y. Liu, T. Pan, L. Zhang, D. Yu, Y. Ge, Kinetic modeling of diffusion mobilities in bcc Ti–Nb alloys, J. Alloys Compd. 476(1-2) (2009) 429-435.

[43] P. George, S.C. Parida, R.G. Reddy, Thermodynamic studies on the system Nb-Al, Metall. Mater. Trans. B, 38 (2007) 85-91.

[44] R. Patterson, Crystal structure of titanium and chromium, Phys. Rev. 26(1) (1925) 56.

[45] P. Duwez, J.L. Taylor, Crystal Structure of TiAl, Jet Propulsion Lab., Pasadena, CA, 1951.

[46] E. Ence, H. Margolin, Compounds in the titanium-rich region of the Ti-Al system, JOM 9(4) (1957) 484-485.

[47] A. Tripathi, K.C.H. Kumar, K.N. Kulkarni, Kinetic modeling of β-BCC phase in Ti–Al–Nb system in the temperature range of 1060–1200 °C, Calphad 68 (2020) 101725.

[48] S. Saha, T. Todorova, J. Zwanziger, Temperature dependent lattice misfit and coherency of Al_3X (X= Sc, Zr, Ti and Nb) particles in an Al matrix, Acta Metall. 89 (2015) 109-115.

[49] C. McKinsey, G. Faulring, A new intermediate phase in the niobium–aluminum system, Acta Crystallogr. 12(9) (1959) 701-702.

[50] C. Colinet, A. Pasturel, D. Nguyen Manh, D. G. Pettifor, P. Miodownik, Phase-stability study of the Al-Nb system, Phys. Rev. B 56 (1997) 552-565.

[51] Y. Mishin, C. Herzig, Diffusion in the Ti–Al system, Acta Mater. 48(3) (2000) 589-623.

[52] D. Konitzer, I. Jones, H. Fraser, Site occupancy in solid solutions of Nb in the intermetallic compounds TiAl and Ti_3Al, Scr. Mater. 20(2) (1986).

[53] Y. Hao, D. Xu, Y. Cui, R. Yang, D. Li, The site occupancies of alloying elements in TiAl and Ti_3Al alloys, Acta Mater. 47(4) (1999) 1129-1139.

2022-12-06

Densification mechanism of Ti-Al-Nb alloys pressurelessly sintered from Al-Nb master alloy powder for cost-effective manufacturing

Liu, Xuzhen

Elsevier

Liu X, Wang J, Li Y, et al., (2023) Densification mechanism of Ti-Al-Nb alloys pressurelessly sintered from Al-Nb master alloy powder for cost-effective manufacturing. Journal of Alloys and Compounds, Volume 936, March 2023, Article number 168307

https://doi.org/10.1016/j.jallcom.2022.168307